Check for updates

Methodological advances for the development of surface engineered carbon nanoarchitectures as a sustainable probe towards high performance hydrogen evolution reaction†

Shokat Hussain, [a] Raheela Akhter, [a] Numan Maroof Butt,[a] Srinibas Beura,[a]
S. M. Nizam Uddin *[ab] and Shrikant S. Maktedar *[a]

In the pursuit of sustainable energy solutions, the development of efficient and environmentally friendly catalysts is crucial. This study focuses on the design and synthesis of Rh@GO electrocatalysts for energy conversion processes, particularly the hydrogen evolution reaction (HER). We introduce three innovative preparation methods: conventional (Rh@GO-SN), solvothermal (Rh@GO-ST), and pyrolysis (Rh@GO-PY). Each method utilizes ultralow amounts of rhodium under distinct conditions of heat and pressure to achieve optimal performance. Rhodium nanostructures are renowned for their exceptional stability, selectivity, and catalytic activity, presenting a promising alternative to traditional platinum-based electrocatalysts. Our results indicate that the synthesized Rh@GO catalysts exhibit significantly enhanced electrocatalytic performance in acidic media for the hydrogen evolution reaction. Key performance metrics include increased current density, reduced overpotential, reduced Tafel slope, and improved stability and durability. Notably, the Rh@GO-PY and Rh@GO-ST catalysts achieve overpotentials of just 31 mV and 38 mV, respectively, at a current density of 10 mA cm^{-2}. This performance surpasses that of the benchmark Pt/C catalyst, which requires an overpotential of 59 mV to reach the same current density.

1. Introduction

The escalating impacts of climate change, primarily driven by extensive fossil fuel combustion, have accelerated the global transition toward sustainable energy solutions. As greenhouse gas emissions continue to rise, the urgency for cleaner, more efficient energy alternatives becomes paramount. This shift is critical not only to mitigate environmental consequences but also to ensure long-term energy security and economic stability. Consequently, the transition from traditional fossil fuel-based energy systems to renewable, carbon-neutral alternatives has become a cornerstone of both scientific research and policy frameworks worldwide.[1,2]

The global demand for energy has seen a relentless increase over the past century, fueled by rapid industrialization, technological advancements, and population growth. By 2050,

energy demand is projected to reach approximately 30 terawatts (TW), far surpassing current generation capacity. This surge in demand underscores the limitations of conventional energy sources, such as coal, oil, and natural gas, which still account for a substantial share of global energy consumption. These sources are not only finite but also contribute significantly to environmental degradation, including air pollution, global warming, and ocean acidification. This reality has accelerated the global quest for alternative energy sources that are both clean and sustainable, capable of meeting future energy needs without exacerbating climate challenges.[3,4]

Among the various candidates for clean energy carriers, molecular hydrogen (H_2) has garnered particular interest due to its high gravimetric energy density and environmentally friendly combustion, producing only water as a byproduct. Hydrogen offers a promising solution for decarbonizing sectors that are traditionally difficult to electrify, such as heavy industry and long-haul transportation. Moreover, it can serve as a versatile energy carrier, allowing for efficient storage and distribution of renewable energy. Despite these advantages, current methods for hydrogen production remain heavily reliant on steam methane reforming (SMR), a process that involves the conversion of natural gas into hydrogen. SMR, while commercially dominant, is energy-intensive and results in significant

[a] *Materials Chemistry & Engineering Research Laboratory, Department of Chemistry, National Institute of Technology, Srinagar-190006, J & K, India. E-mail: shrikant@nitsri.ac.in*

[b] *Department of Chemistry, Graduate School of Physical Sciences, Shahjalal University of Science and Technology, Sylhet-3114, Bangladesh. E-mail: sohel-che@sust.edu*

CO_2 emissions, undermining the potential environmental benefits of hydrogen as a clean fuel. Consequently, there is a critical need for alternative hydrogen production methods that are sustainable, efficient, and economically viable.

Electrochemical water splitting has emerged as a promising approach to produce hydrogen in a carbon-neutral manner. This process involves the electrolysis of water into hydrogen and oxygen using renewable electricity, offering a pathway for the large-scale production of green hydrogen. The efficiency of this process hinges on the performance of electrocatalysts, which facilitate the hydrogen evolution reaction (HER) and oxygen evolution reaction (OER)—the two key half-reactions in water splitting. Effective electrocatalysts can lower the activation energy for these reactions, thereby reducing the energy input required for hydrogen production. This makes the development of advanced electrocatalysts a critical research focus for achieving economically viable hydrogen production.[5–7]

Traditional electrocatalysts for the HER, particularly those based on platinum-group metals (PGMs), are highly efficient but face limitations due to their high cost and scarcity. Rhodium (Rh), another PGM, has demonstrated exceptional catalytic activity and stability in various electrochemical reactions, making it a promising alternative to platinum. However, the challenge lies in reducing the reliance on these precious metals while maintaining high catalytic performance. One strategy to address this involves synthesizing rhodium-based nanostructures with minimal metal loading, optimized for maximum catalytic activity and stability.[8–12]

In this context, rhodium-decorated graphene oxide (Rh@GO) nanocomposites have emerged as a compelling solution. Graphene oxide serves as an ideal support due to its large surface area, high electrical conductivity, and ability to stabilize metal nanoparticles, thus enhancing the dispersion and utilization of Rh atoms. The integration of Rh with GO aims to synergistically improve the electron transfer kinetics and catalytic efficiency of the composite material. Notably, Rh@GO composites have demonstrated enhanced electrocatalytic activity for the HER, with reduced overpotentials and improved stability compared to conventional catalysts.[13,14]

This study introduces a novel approach to the synthesis of Rh@GO nanocomposites by exploring three distinct preparation methods: conventional synthesis (Rh@GO-SN) involves a straightforward chemical reduction process to deposit Rh nanoparticles onto GO. This method offers simplicity and ease of implementation, allowing for the efficient production of Rh@GO composites. Solvothermal synthesis (Rh@GO-ST) utilizes elevated temperature and pressure conditions in a sealed environment to control the size and distribution of Rh nanoparticles. This technique enables precise manipulation of nanoparticle characteristics, leading to uniform dispersion and enhanced catalytic properties. Pyrolysis (Rh@GO-PY) involves high-temperature treatment under an inert atmosphere to enhance the crystallinity and interfacial interactions between Rh and GO. This process aims to improve the structural integrity and durability of the electrocatalyst.

The novelty of this work lies in the systematic comparison of these synthesis routes to elucidate the relationship between preparation methods, structural properties, and catalytic performance. By tailoring the synthesis parameters, this study seeks to optimize the design of Rh@GO electrocatalysts, achieving high efficiency with minimal Rh loading. Such an approach addresses the critical challenge of reducing reliance on scarce and expensive PGMs while maintaining superior catalytic activity.

Each of the three synthesis methods offers unique advantages that justify their exploration. Conventional synthesis (Rh@GO-SN) provides a baseline for comparison, offering insights into the fundamental interactions between Rh nanoparticles and GO without the influence of complex processing conditions. Solvothermal synthesis (Rh@GO-ST) allows for precise control over nanoparticle morphology and distribution, which are critical factors influencing catalytic activity. The solvothermal method's ability to produce uniform nanoparticles with tailored properties makes it a valuable technique for optimizing electrocatalyst performance. The pyrolysis method (Rh@GO-PY) employs high-temperature treatment under an inert atmosphere, enhancing the crystallinity of Rh nanoparticles and strengthening their interaction with the GO support. This process aims to improve the structural integrity and durability of the electrocatalyst, leading to superior performance in HER applications. Such thermal treatments can result in catalysts with enhanced activity and stability due to improved electronic properties and stronger metal–support interactions. By systematically comparing these three synthesis methods, this study seeks to elucidate the relationship between preparation techniques, structural properties, and catalytic performance of Rh@GO nanocomposites. The goal is to optimize the design of cost-effective, high-performance electrocatalysts for sustainable hydrogen production, contributing to the advancement of clean energy technologies.

The innovative synthesis methods explored in this study offer distinct pathways to engineer Rh@GO nanocomposites with tailored structural and catalytic properties. By systematically comparing these methods, our work provides critical insights into how synthesis parameters influence the dispersion, particle size, and interaction between Rh nanoparticles and the GO support, directly impacting the electrocatalytic performance. This comprehensive approach not only advances the understanding of Rh@GO systems but also contributes significantly to the broader field of catalyst design for sustainable energy applications. The implications of this research are far-reaching, offering a viable strategy to reduce dependence on scarce and expensive platinum-group metals, thereby lowering costs and promoting the scalability of hydrogen production technologies. Ultimately, the development of efficient, durable, and cost-effective Rh@GO electrocatalysts has the potential to accelerate the transition toward a hydrogen-based energy economy, addressing critical challenges in energy security and environmental sustainability.

2. Experimental section

The details about the materials and reagents used, instruments and techniques used for materials characterization, electrode

preparation and electrochemical measurements, and calculations are provided in Sections S1, S2, S3, and S4, respectively, of the ESI.†

2.1. Materials synthesis

2.1.1. Synthesis of graphene oxide.
Graphene oxide (GO) was synthesized using a modified Hummers' method.[15,16] Briefly, 5 g of graphite powder was added to 230 mL of 98% H_2SO_4 and 5 mL of 78% HNO_3, and the mixture was stirred for 4 hours. Following this, 30 g of $KMnO_4$ was added while maintaining an ice bath and continuous stirring for 1 hour. The mixture was then heated to 35 °C and stirred for another hour. Subsequently, 450 mL of deionized water (DW) was added slowly, ensuring that the ice bath was maintained due to the exothermic nature of the reaction, until the mixture reached room temperature. The reaction mixture was then heated to 95–98 °C for 2 hours, keeping in mind that it should not boil. After turning off the heat, the mixture was allowed to cool naturally to room temperature. At this point, 1 liter of DW and 100 mL of H_2O_2 were added, followed by stirring for 1 hour. The solution was left overnight to settle. The supernatant was decanted, and the remaining mixture was centrifuged and washed first with 30% HCl (2–3 times) and then with DW (4–5 times) until the pH of the residue was neutral. The extract was then placed in a Petri dish and dried in a vacuum oven at approximately 60 °C for 2–3 days. The dried GO was used for structural and morphological characterizations before electrochemical and electrocatalytic studies.

2.1.2. Synthesis of Rh@GO.
Three different methods were used for the synthesis of the Rh@GO nanocomposite: high-temperature pyrolysis, solvothermal synthesis, and the conventional approach.

2.1.2.1. Conventional synthesis of Rh@GO. A total of 800 mg of acid-functionalized GO powder was dissolved in 200 mL of hot anhydrous ethylene glycol, and 80 mg of rhodium acetate was added. This mixture was sonicated for one hour, and then heated at 160 °C for six hours. After cooling naturally to room temperature, the mixture was filtered using a PTFE membrane with a 0.2-μm pore size to remove any remaining ethylene glycol, unreacted rhodium acetate, and other impurities. The residue was redispersed and washed several times with acetone. The resulting Rh@GO-SN composite was then dried in an oven at 100 °C for one hour to eliminate any remaining solvent molecules. This composite material was subsequently used for further characterization and electrochemical research.

2.1.2.2. Solvothermal synthesis of Rh@GO. The solvothermal Rh@GO nanocomposite was prepared by dissolving 800 mg of acid-functionalized GO powder in 200 mL of preheated anhydrous ethylene glycol. Then, 80 mg of Rh acetate was added, and the mixture was sonicated for one hour. The reaction mixture was placed in an autoclave and heated at 160 °C in a furnace for six hours. Afterward, the mixture was filtered using Whatman filter paper and washed with acetone 4–5 times. The resulting Rh@GO-ST composite was dried in an oven at 100 °C

for one hour to remove solvent molecules. This composite material was subsequently used for further characterization and electrochemical studies.

2.1.2.3. Pyrolysis based synthesis of Rh@GO. The synthesis of the Rh@GO-PY nanocomposite can be achieved by modifying the basic pyrolysis process. Graphene and rhodium acetate, in a 9:1 ratio, were mixed by ball milling for about 4 hours at 500 rpm. The mixture was then placed in a Teflon boat inside a tube furnace. An inert atmosphere was maintained by introducing argon gas for 4 hours while heating the sample to 800 °C at a scan rate of 5 °C per minute. This composite material was subsequently used for further characterization and electrochemical studies.

All the three methods are summarized in Table S1 of the ESI† and represented in Scheme 1.

3. Results and discussion

3.1. Materials characterization

The crystal phase analysis was conducted using the X-ray diffraction (XRD) technique. Fig. 1(a) contrasts the XRD signatures of the pristine GO and Rh@GO (Rh@GO-PY, Rh@GO-ST, and Rh@GO-SN) catalysts. As seen, the pristine GO exhibits a sharp peak at 10.4°, corresponding to the (100) plane, indicating the formation of the graphite oxide structure and the disappearance of a peak at $2\theta = 26.6°$. The transformation of graphite into graphite oxide resulted in a shift to the left, signifying the successful oxidation of graphite.[17] GO also shows a weak, broad peak around 22°–27°, which has nearly one-eighth of the integrated intensity of the main GO peak. This peak suggests that the framework of the sample comprises few-layer stacked graphene nanosheets and is attributed to the (002) plane.[18] In the case of Rh@GO-PY, Rh@GO-ST, and Rh@GO-SN, the broad peak located at $2\theta = 24°–27°$ is attributed to the (002) peak of stacked reduced graphene oxide (rGO) sheets, indicating that the GO has been reduced to rGO.[19] Additionally, other new diffraction peaks, appearing at 41.05°, 47.77°, 69.87°, and 84.39° for Rh@GO-PY, at 40.96°, 47.71°, 69.75°, and 84.39° for Rh@GO-ST, and at 41.03°, 47.67°, 69.95°, and 84.39° for Rh@GO-SN, could be attributed to the (111), (200), (220), and (311) planes of the face-centered cubic (FCC) Rh crystal (DB Card No. Rh@GO-PY = 03-065-2866, Rh@GO-ST = 00-005-0685, and Rh@GO-SN = 01-072-3120) with a space group of 225: $Fm\bar{3}m$, respectively, indicating the high purity of the as-prepared catalysts.[20,21] Table 1 presents the various parameters obtained from the XRD analysis of the materials.

The as-synthesized Rh@GO catalysts and GO were further examined using Raman scattering spectroscopy. Fig. 1(b) displays the Raman spectra of the GO and Rh@GO (Rh@GO-PY, Rh@GO-ST, and Rh@GO-SN) catalysts. As shown, two primary vibrations are observed in the range of 1100 and 1700 cm^{-1} for GO. The D vibration band, resulting from a breathing mode of *j*-point photons of A_{1g} symmetry,[22] is seen at 1348.87 for GO. Conversely, the G vibration band, from first-order scattering of E_{2g} phonons by sp^2 carbon,[22] appears at 1592.01 for GO. Moreover, the G vibration band is also influenced by the presence of the stretching C–C bond, which is typical in all
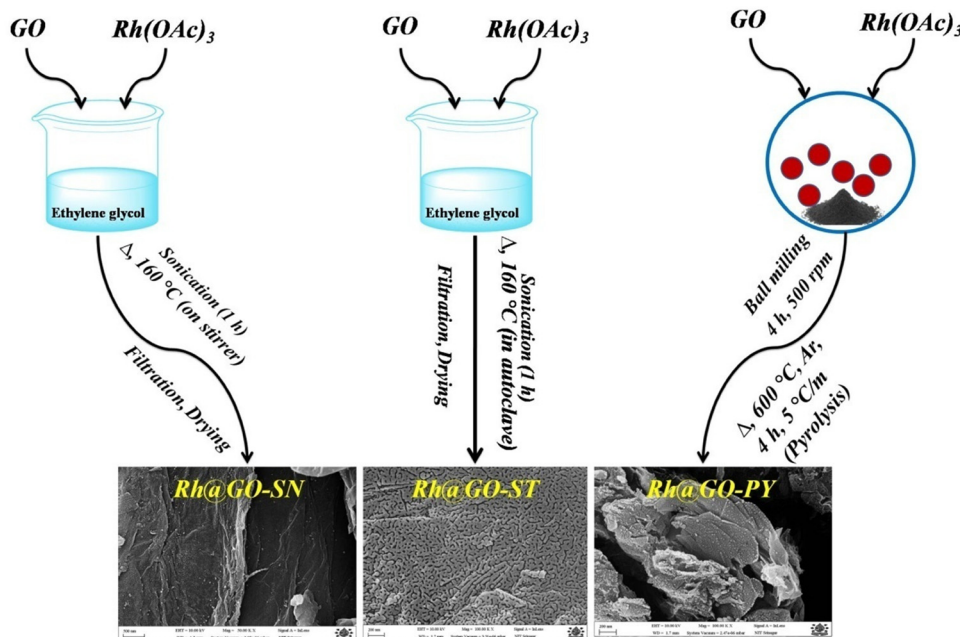
Scheme 1 Schematic representation of the synthesis of Rh@GO-SN, Rh@GO-ST and Rh@GO-PY.

sp^2 carbon systems.[23] The D band and G band in the Raman spectrum represent the disorder bands and the tangential bands, respectively.[24] Additionally, a broad and shifted-to-higher-wavenumber 2D band is observed at 2761.24 cm^{-1} for GO. The 2D band is crucial for determining the layers of graphene (monolayer, double layer, or multilayer) as it is highly sensitive to the stacking of graphene layers.[22] Therefore, the position of the 2D band confirms that the produced GO is multilayer since monolayer graphene is typically observed at 2679 cm^{-1} in the spectrum.[23] The shifted location of the 2D band is also due to the presence of oxygen-containing functional groups that prevent the graphene layers from stacking.[22] The I_D/I_G ratio for GO was found to be 0.85, and the I_{2D}/I_G ratio was 0.02. In the case of Rh@GO catalysts, the two main peaks at about 1342.97 cm^{-1} and 1587.54 cm^{-1} for Rh@GO-PY, 1348.99 cm^{-1} and 1599.58 cm^{-1} for Rh@GO-ST, and 1342.97 cm^{-1} and 1587.54 cm^{-1} for Rh@GO-SN, correspond to the typical D and G bands, respectively. A much broader peak of a 2D band is also present in the Rh@GO catalysts, indicating the stacking of rGO with a few layers. The I_D/I_G ratio for Rh@GO-PY, Rh@GO-ST, and Rh@GO-SN was determined to be 0.95, 1.08, and 1.10, respectively. The increased ratio suggests enhanced disorder in the graphene due to the interactions between GO and Rh, which may be beneficial for electrocatalysis.[20] These results also confirm the *in situ* conversion of GO into rGO during catalyst formation. It is established that the I_D/I_G ratio indicates the degree of defects present in the rGO samples, while the I_{2D}/I_G ratio reflects the recovery of the sp^2 C=C bond in the graphitic structure and hole mobility.[25] A lower I_D/I_G ratio indicates fewer defects, and a higher I_{2D}/I_G ratio indicates higher charge mobility.[26] The I_{2D}/I_G ratio for Rh@GO-PY, Rh@GO-ST, and Rh@GO-SN was determined to be 0.22, 0.23, and 0.1, respectively.

The FT-IR spectra of the GO and Rh@RGO catalysts (Rh@GO-PY, Rh@GO-ST, and Rh@GO-SN) shown in Fig. 1(c) reveal strong signals for GO at 3741, 1710, and 1654 cm^{-1}, corresponding to OH, C=O, and C=C stretching frequencies, respectively. These signals are typical indicators of oxidative functional groups such as OH and COOH, confirming the formation of GO. Additionally, the signals at 672 cm^{-1} (Rh–O) and 1024 cm^{-1} (C–O) indirectly confirm the formation of the Rh–GO nanocomposite. The peaks around 2835 and 2880 cm^{-1} are attributed to the asymmetric and symmetric vibrations of C–H stretching frequencies, respectively, which align well with the literature.[21,27–30]

Fig. 2 presents the SEM images of Rh@GO (Rh@GO-PY, Rh@GO-ST, and Rh@GO-SN). Fig. S1(a) and (b) of the ESI† show the SEM images of graphene oxide at various magnifications, confirming the successful formation of GO flakes and layers in the form of thin sheets.[31] Fig. 2(a)–(c) depicts the SEM images of Rh@GO-SN, revealing the morphology of rGO sheets with Rh nanospheres decorating the surface and interlayer spaces. It also confirms that the rGO layers are well-separated and uniformly decorated with Rh nanospheres, with a particle size of approximately 8.01 nm.[30,32] Fig. 2(d)–(f) displays the SEM images of Rh@GO-ST, showing rGO sheets with lamellar-shaped Rh nanoparticles on the surface and between layers. These lamellar Rh nanostructures are homogeneously distributed, with a particle size of around 45.03 nm.[33] Fig. 2(g)–(i) shows the SEM images of Rh@GO-PY, indicating well-separated rGO sheets that result in small pores between them. The Rh nanoparticles, in the form of small nanospheres, are finely distributed and uniformly decorate the surface, interlayers, and small pores, with a particle size of approximately 12.25 nm.[19,34]

To understand the chemical composition and elemental distribution, EDS study of the materials was conducted.
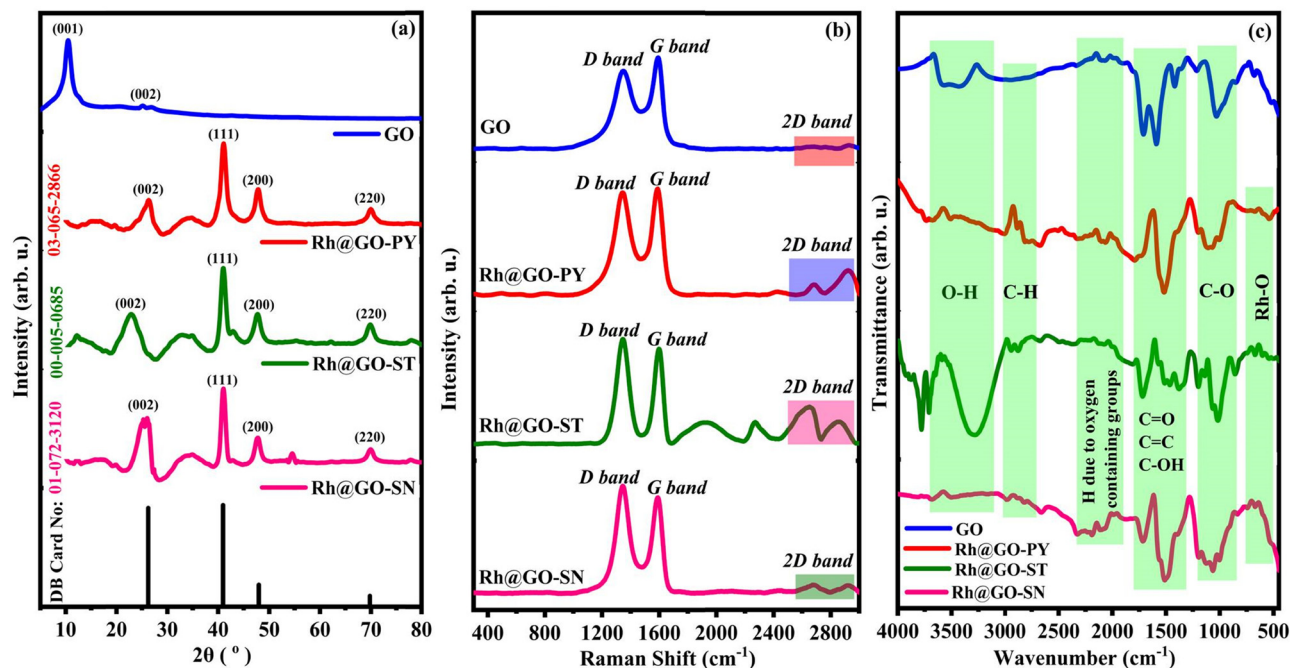
Fig. 1 XRD patterns, Raman spectra and FTIR spectra of GO and Rh@GO catalysts: (a) XRD spectra of GO, Rh@GO-PY, Rh@GO-ST and Rh@GO-SN, (b) Raman spectra of GO, Rh@GO-PY, Rh@GO-ST and Rh@GO-SN, and (c) FTIR spectra of GO, Rh@GO-PY, Rh@GO-ST and Rh@GO-SN.

The elemental composition, weight%, and atomic% of Rh@GO-PY, Rh@GO-ST, and Rh@GO-SN are shown in Fig. S2 of the ESI.†

Fig. 3 presents a comparative transmission electron microscopy (TEM) and selected area electron diffraction (SAED) analysis of the Rh@GO electrocatalysts (Rh@GO-PY, Rh@GO-ST and Rh@GO-SN). The Rh@GO-PY (Fig. 3(a)–(c)) shows an excellent dispersion of Rh nanoparticles across the graphene oxide sheets. Low-magnification TEM reveals a uniform distribution with minimal aggregation, while medium-magnification images show nanoparticles that are small, spherical, and relatively monodisperse, typically below 10 nm. High-resolution TEM confirms the polycrystalline nature of the Rh nanoparticles, with clear lattice fringes corresponding to the (111) and (002) planes. The SAED pattern (Fig. 3(d)) further supports this, showing sharp and well-defined diffraction rings indexed to the (111), (220), and (002) planes of face-centered cubic Rh and partially reduced GO confirming its polycrystalline nature. The high crystallinity and uniform morphology suggest strong metal–support interactions and controlled nanoparticle formation due to the thermal conditions of pyrolysis. This makes Rh@GO-PY highly suitable for catalytic applications where uniform particle size and high crystallinity are critical. The Rh@GO-ST sample (Fig. 3(e)–(g)) displays moderately well-dispersed Rh nanoparticles with noticeable aggregation. TEM images at low magnification show particle distribution on the GO surface, but with the presence of some larger clustered domains. Medium-magnification TEM reveals nanoparticles that are generally larger and more polydisperse compared to Rh@GO-PY. High-resolution TEM still shows clear lattice fringes with d-spacing values consistent with the (111) and (002) planes, indicating the presence of crystalline Rh on partially reduced GO. The SAED pattern (Fig. 3(h)) confirms this with visible but slightly less intense diffraction rings for the (111), (220), and (002) lattice planes of Rh and partially reduced GO and which shows its single crystalline nature. The solvothermal method appears to provide good crystallinity, but less control over particle size and dispersion, likely due to slower nucleation and growth processes. This sample may be suitable for catalytic or electrochemical applications where slightly larger nanoparticles are acceptable or desirable. The Rh@GO-SN sample (Fig. 3(i)–(k)) exhibits the least uniform nanoparticle dispersion among the three methods. TEM analysis at low and medium magnification

Table 1 Parameters of crystal structure obtained from XRD analysis of Rh@GO-PY, Rh@GO-ST and Rh@GO-SN

Parameters	Rh@GO-PY	Rh@GO-ST	Rh@GO-SN
Crystallite size (D) (nm) (Scherrer equation)	6.50	5.01	6.44
Strain (%) (Williamson–Hall method)	0.4	0.0	0.0
Crystallinity (%)	78.97	69.31	70.27
DB card no.	03-065-2866	00-005-0685	01-072-3120
$a = b = c$	3.80	3.81	3.80
$\alpha = \beta = \gamma$	90°	90°	90°
Crystal system	FCC	FCC	FCC
Space group	225: $Fm\bar{3}m$	225: $Fm\bar{3}m$	225: $Fm\bar{3}m$

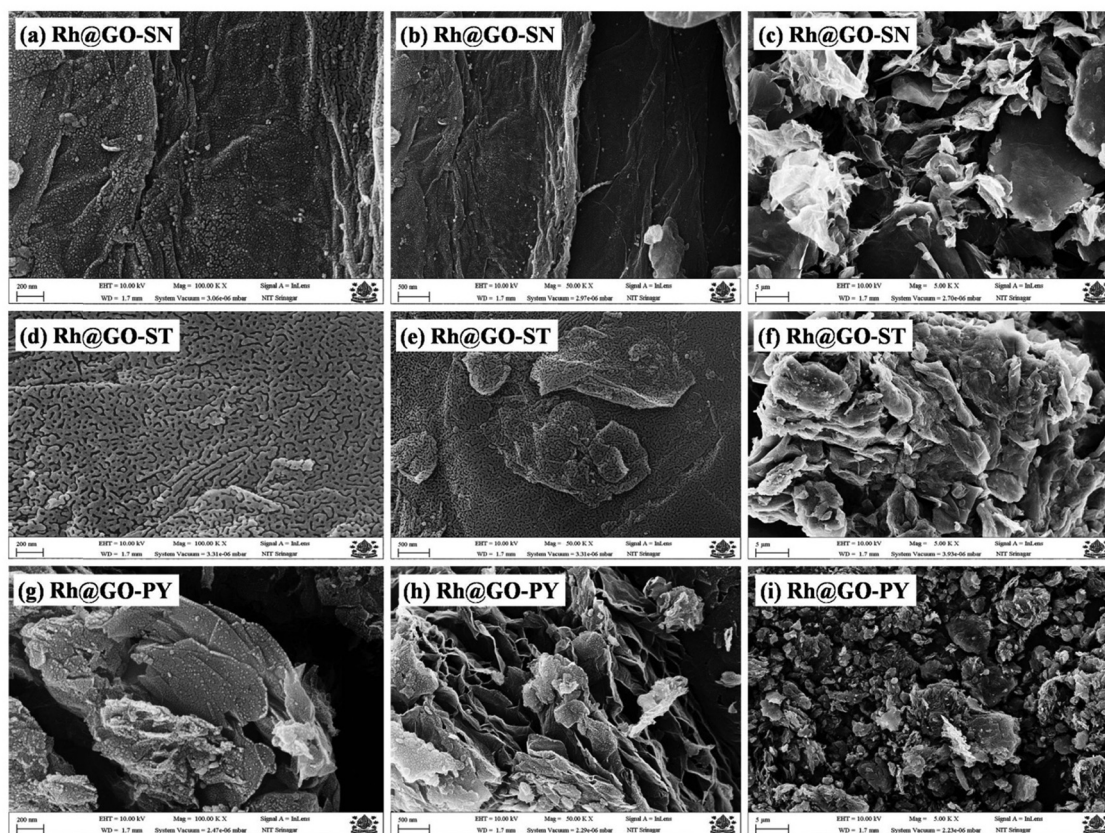|	Rh@GO-PY		Rh@GO-ST		Rh@GO-SN	
Parameters	2θ (°)	d (Å)	2θ (°)	d (Å)	2θ (°)	d (Å)
d-Spacing	26.23	3.394	22.82	2.1702	25.39	3.504
	41.05	2.1966	40.96	2.2015	41.03	2.197
	47.77	1.9023	47.71	1.9048	47.67	1.905
	69.87	1.3452	69.75	1.3472	69.95	1.343

Fig. 2 SEM images of Rh@GO catalysts at different magnifications: (a) Rh@GO-SN at 200 nm, (b) Rh@GO-SN at 500 nm, (c) Rh@GO-SN at 5 μm, (d) Rh@GO-ST at 200 nm, (e) Rh@GO-ST at 500 nm, (f) Rh@GO-ST at 5 μm, (g) Rh@GO-PY at 200 nm, (h) Rh@GO-PY at 500 nm, and (i) Rh@GO-PY at 5 μm.

shows a heterogeneous distribution with significant nanoparticle clustering and irregular shapes. The particles are larger and highly polydisperse, lacking the uniformity observed in the PY and ST methods. High-resolution TEM does reveal lattice fringes, confirming the presence of crystalline Rh, but the fringes are less distinct, suggesting partial disorder or smaller crystalline domains. The SAED pattern (Fig. 3(l)) presents diffuse rings corresponding to the (111), (220), and (002) planes, indicating polycrystalline structures with a more amorphous background. This reduced structural order and weaker dispersion can be attributed to the lower energy input and shorter reaction times characteristic of sonication. While the sonochemical method is simple and rapid, it offers the least control over nanoparticle formation, making Rh@GO-SN less ideal for applications requiring fine-tuned nanostructures, though it could be useful for bulk catalytic processes or as a low-cost material. Overall, the results in all the three catalysts are in agreement with the XRD pattern, which further confirms the successful incorporation and dispersion of Rh nanoparticles on and inside the partially reduced GO sheets resulting in the synthesis of Rh@GO electrocatalysts.[19,20,35]

The catalytic performance of electrocatalysts is primarily influenced by their surface composition. To investigate the chemical makeup and surface atomic electronic structures of the Rh@GO electrocatalysts and GO, XPS was conducted. Fig. 4 presents the XPS spectra of graphene oxide (GO). As illustrated in Fig. 4(a), the XPS survey spectrum confirms the presence of

carbon (C) and oxygen (O) as the primary elements in GO, consistent with the EDX findings. The atomic percentages derived from the survey spectrum indicate high oxygen content, reflecting the substantial oxidation of graphite during GO synthesis. The high-resolution C1s spectrum (Fig. 4(b)) reveals three deconvoluted peaks at 284.88, 286.88, and 288.63 eV, which correspond to C=C (sp²-hybridized carbon), C–O (epoxy/hydroxyl groups), and C=O (carbonyl groups), respectively. This distribution indicates the presence of various oxygenated functional groups characteristic of GO, confirming successful oxidation. The dominant C–O and C=O peaks highlight the disruption of the graphitic structure and the introduction of oxygen functionalities. Fig. 4(c) shows the O1s high-resolution spectrum, exhibiting peaks at 532.68 and 534.95 eV, corresponding to oxygen in C–O and C=O environments, respectively. The relatively higher intensity of the C–O peak compared to C=O suggests that hydroxyl and epoxy groups are more prevalent in the GO structure. These features are essential for subsequent reduction and functionalization steps, as they serve as anchoring sites for metal ions and reducing agents.[19,30,36–39]

Fig. 5 illustrates the XPS spectra of the Rh@GO-PY nanocomposite. In the survey spectrum (Fig. 5(a)), Rh, C, and O are clearly observed, verifying the successful loading of Rh nanoparticles and agreeing with the EDS results. The high-resolution C1s spectrum (Fig. 5 (b)) shows two peaks at 284.45 and 285.19 eV, assigned to sp² C–C/C=C and C–O
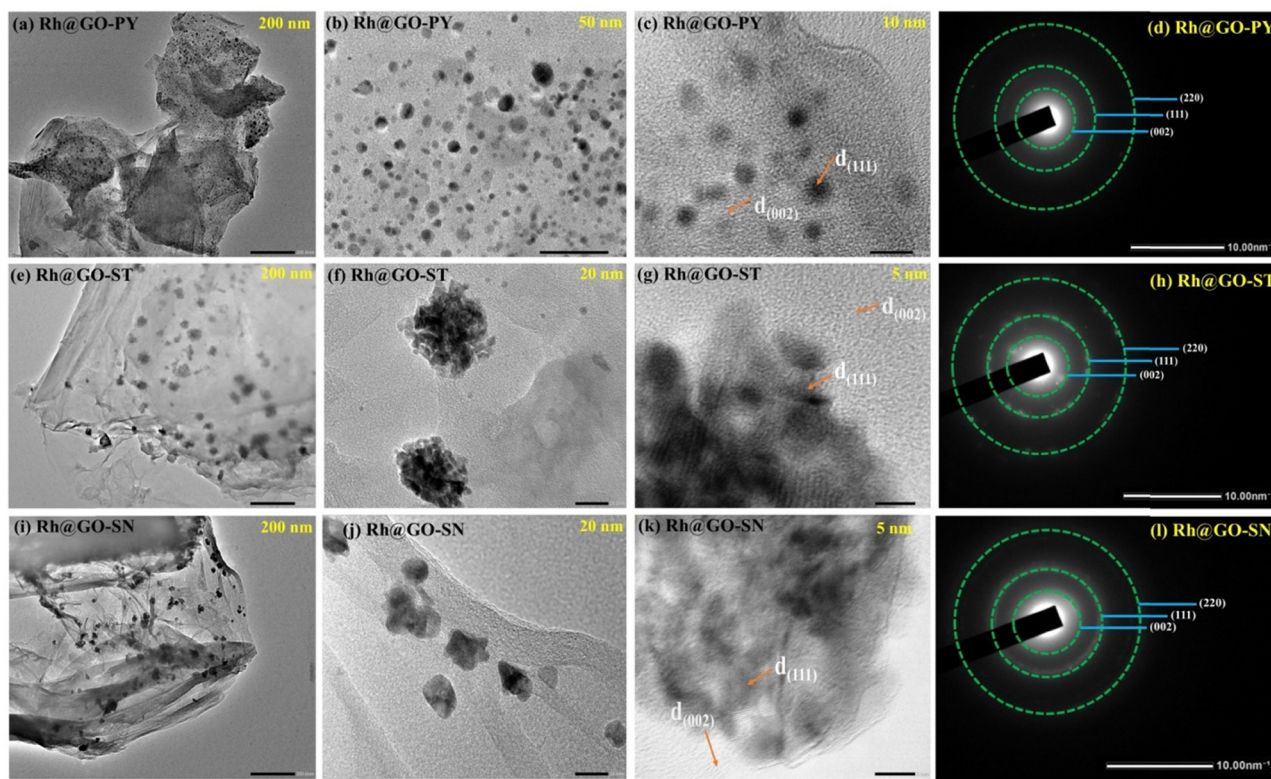
Fig. 3 HR-TEM and SAED patterns of Rh@GO electrocatalysts: (a) HR-TEM of Rh@GO-PY at 200 nm, (b) HR-TEM of Rh@GO-PY at 50 nm, (c) HR-TEM of Rh@GO-PY at 10 nm, (d) SAED of Rh@GO-PY, (e) HR-TEM of Rh@GO-ST at 200 nm, (f) HR-TEM of Rh@GO-ST at 20 nm, (g) HR-TEM of Rh@GO-ST at 5 nm, (h) SAED of Rh@GO-ST, (i) HR-TEM of Rh@GO-SN at 200 nm, (j) HR-TEM of Rh@GO-SN at 20 nm, (k) HR-TEM of Rh@GO-SN at 5 nm, and (l) SAED of Rh@GO-SN.

bonds, respectively. Compared to GO, the absence of a significant C=O peak and a shift in the C–O peak suggest partial reduction of GO during Rh incorporation. This implies that Rh precursors or the synthesis process itself facilitated *in situ* chemical reduction, restoring some graphitic domains and enhancing electrical conductivity. The O1s spectrum (Fig. 5(c)) contains two peaks at 532.29 and 533.78 eV, which represent C–O and C=O bonds, respectively. The reduced intensity of these peaks, compared to GO, further confirms the partial reduction of GO during the composite formation. The Rh 3d spectrum (Fig. 5(d)) shows two main peaks at 307.28 eV and 312.08 eV,

attributed to Rh $3d_{5/2}$ and Rh $3d_{3/2}$ levels of metallic Rh^0, respectively. The binding energy (BE = 4.9 eV) is in agreement with literature values for elemental rhodium, confirming the metallic state of the Rh nanoparticles. The narrow peak width and absence of Rh^{3+} species suggest successful reduction and minimal oxidation of Rh during synthesis.[19,30,36–39]

The XPS spectra of Rh@GO-SN are shown in Fig. 6. The survey spectrum (Fig. 6(a)) confirms the presence of Rh, C, and O. The C1s spectrum (Fig. 6(b)) reveals peaks at 284.47 and 285.46 eV, corresponding to C–C/C=C and C–O, respectively. The C=O peak is not prominent, indicating more complete
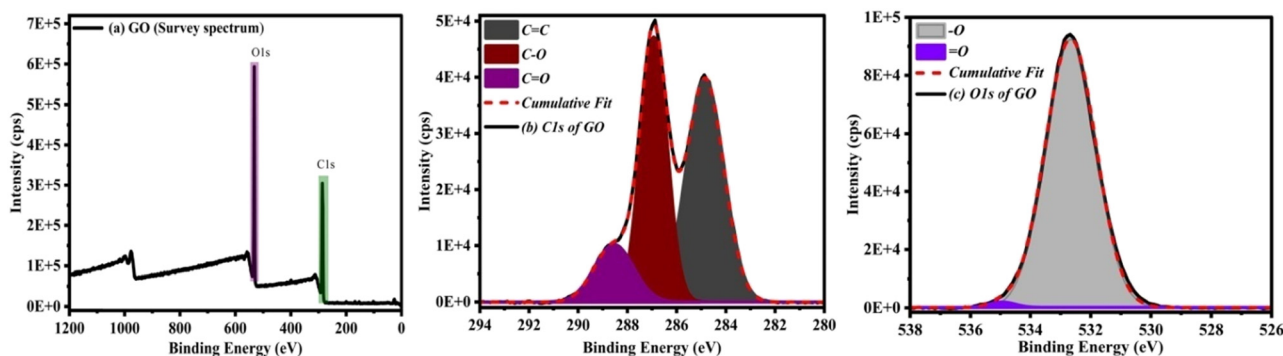
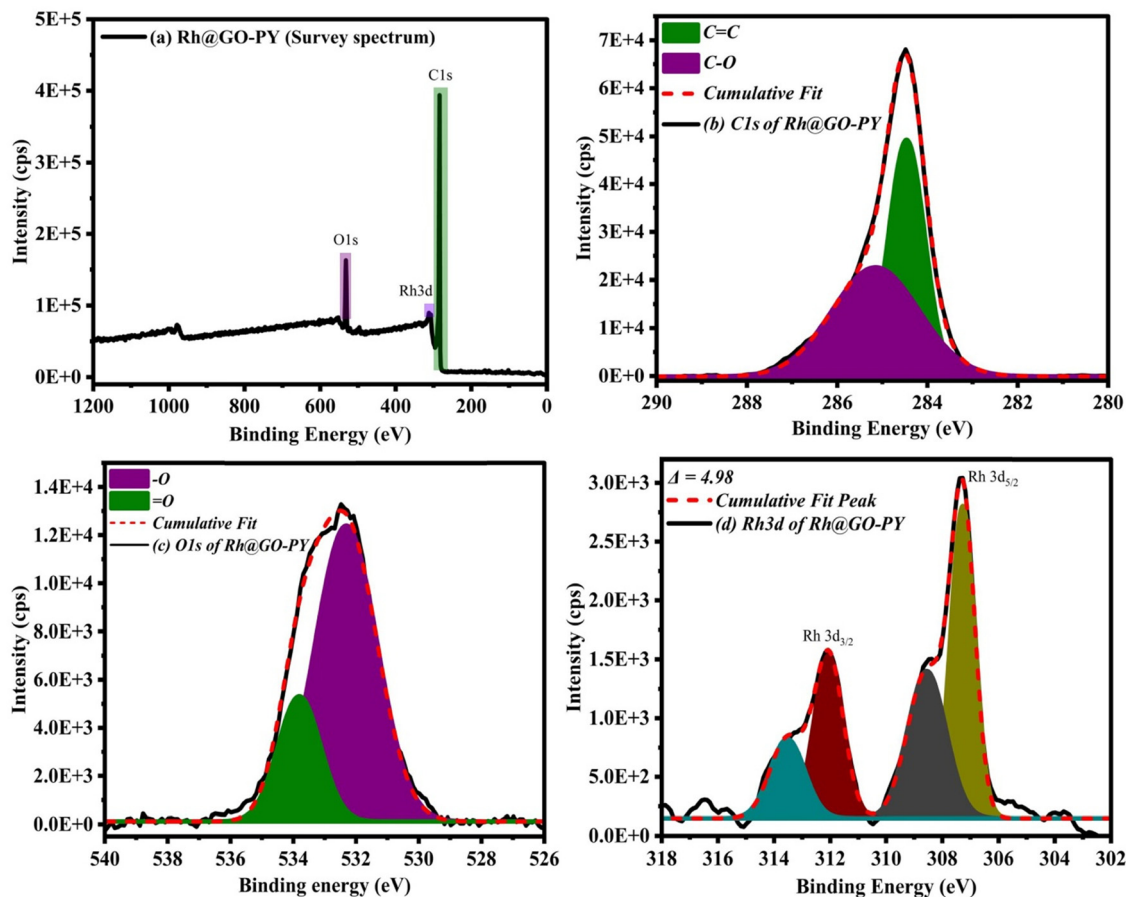**Fig. 4** XPS spectra of GO: (a) survey spectrum, (b) C1s region, and (c) O1s region.

Fig. 5 XPS spectra of Rh@GO-PY: (a) survey spectrum, (b) C1s region, (c) O1s region, and (d) Rh 3d region.

reduction compared to GO, similar to Rh@GO-PY. In Fig. 6(c), the O1s spectrum reveals peaks at 531.72 and 533.24 eV, attributed to C–O and C=O species, respectively. The peak shifts and lower intensities imply that most oxygenated groups have been reduced, possibly due to the reducing environment created by SN during synthesis. The Rh 3d spectrum in Fig. 6(d) shows BE values at 307.28 and 312.13 eV for Rh $3d_{5/2}$ and $3d_{3/2}$, respectively, with a BE of 4.9 eV. This confirms the metallic state of Rh, as observed in Rh@GO-PY, and indicates stable binding of Rh nanoparticles in the GO matrix without oxidation.[19,30,36–39]

The XPS spectra of Rh@GO-ST are displayed in Fig. 7. The survey spectrum (Fig. 7(a)) confirms the presence of Rh, C, and O. Notably, in Fig. 7(b), the C1s high-resolution spectrum shows three distinct peaks at 284.44, 285.51, and 288.42 eV, corresponding to C–C/C=C, C–O, and C=O bonds, respectively. The reappearance of the C=O peak suggests less effective reduction of GO in this synthesis, indicating that the ST additive provided weaker reducing power or led to partial oxidation post-synthesis. The O1s spectrum (Fig. 7(c)) shows peaks at 532.56 and 534.60 eV, confirming the retention of oxygen functionalities, possibly due to incomplete reduction or re-oxidation during or after synthesis. Interestingly, the Rh 3d spectrum in Fig. 7(d) presents slightly shifted peaks at 306.09 and 312.19 eV for Rh $3d_{5/2}$ and Rh $3d_{3/2}$, respectively, with a BE

of 5.5 eV. The increased BE may indicate slight electronic interactions between Rh and oxygenated groups or charge transfer between Rh and the GO matrix. This suggests a possible variation in the chemical environment or coordination of Rh in Rh@GO-ST compared to other composites.[19,30,36–39]

To estimate thermal stability and phase transformation, thermogravimetric analysis (TGA) studies were conducted within the temperature ranges of 30–750 °C for the GO and Rh@GO catalysts (Rh@GO-PY, Rh@GO-ST, and Rh@GO-SN) in an N_2 inert atmosphere, with the respective thermograms presented in Fig. 8. The gradual weight loss of about 26% for GO in the 30–180 °C range is attributed to the decomposition of oxidative functional groups, and a rapid weight loss up to 96.94% occurs between 180–200 °C due to the oxidative decomposition of graphene to carbon dioxide. Thus, GO is thermally stable within the 30–180 °C range, but starts to decompose rapidly beyond 180 °C, reaching a weight loss of 96.94% at 200 °C and up to 99.9% at the given temperature. For Rh@GO, the weight loss was only 27%, 28%, and 39% for Rh@GO-SN, Rh@GO-PY and Rh@GO-ST, respectively, at the given temperature. As shown in Fig. 3(b), the Rh@GO catalysts exhibited slow thermal decomposition with minimal weight loss, likely due to the decomposition of GO from Rh–GO, where Rh acts as a catalyst for the decomposition at a low temperature. From dTG analysis, thermal decomposition was found to occur in one
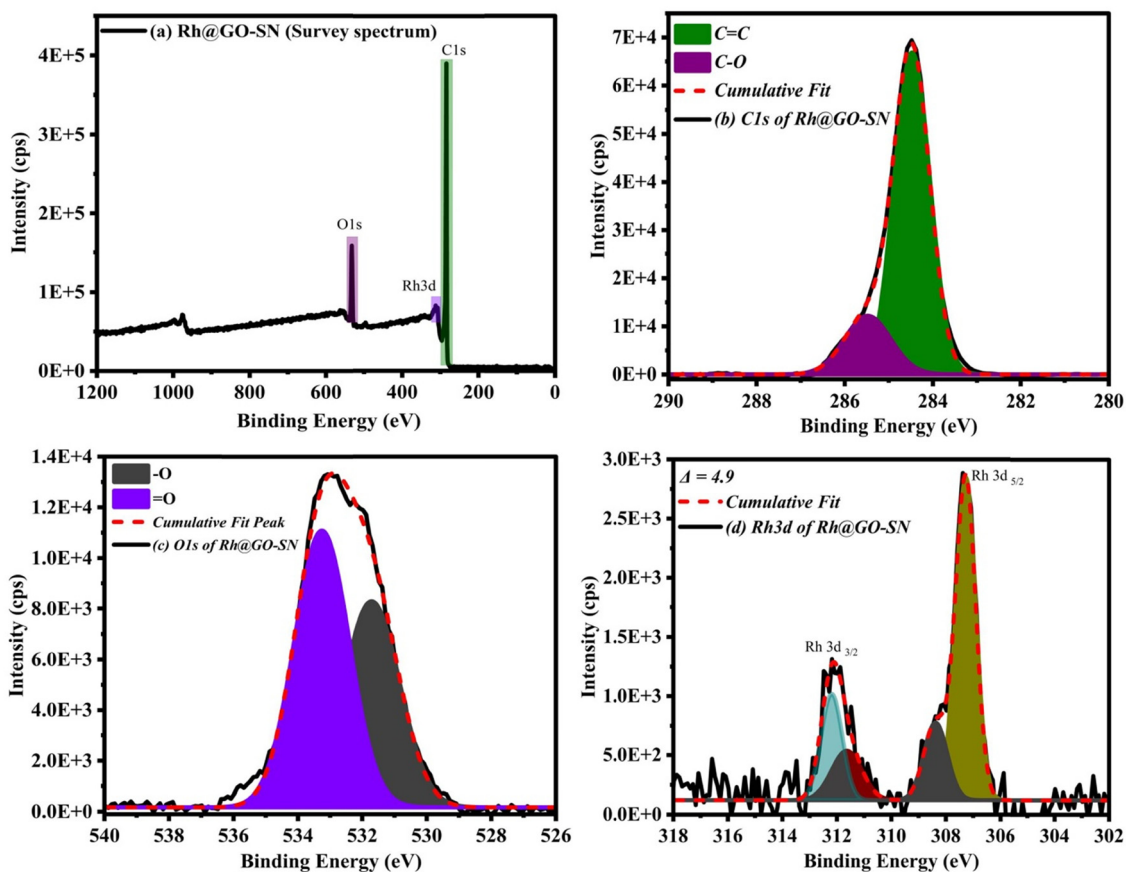
Fig. 6 XPS spectra of Rh@GO-SN: (a) survey spectrum, (b) C1s region, (c) O1s region, and (d) Rh 3d region.

stage at 190 °C for GO, and in three stages at 42 °C, 150 °C, and 342 °C for Rh@GO-SN, at 79 °C, 160 °C, and 319 °C for Rh@GO-ST, and in two stages at 280 °C and 450 °C for Rh@GO-PY. These results indicate that the thermal stability order of Rh@GO catalysts is Rh@GO-SN > Rh@GO-PY > Rh@GO-ST.[40–45]

3.2. Electrochemical analysis

To investigate the activity of the electrocatalysts in controlled-potential techniques, it is crucial to examine the electronic conductivity of the electrocatalyst and the potential drop at the working electrode–electrolyte interface.[46] The electrochemical impedance spectroscopy (EIS) technique was used to investigate the uncompensated resistance (R_u) of the system and the charge transfer resistance (R_{ct}) of the electrode surfaces. Fig. 9(a) represents the normalized Nyquist plots of Rh, GO, Pt/C, Rh@GO-SN, Rh@GO-ST and Rh@GO-PY modified GC electrode surfaces in the frequency range of 0.1 Hz to 0.1 MHz at their open circuit potentials in 0.1 M H_2SO_4 solution. It displays the distinct semicircles for each modified electrode, indicating that the uncompensated resistance (R_u) is in series with the parallel combination of constant phase element (CPE) and charge transfer resistance (R_{ct}) on each electrode surface. The diameter of the semicircles in the Nyquist plots represents the R_{ct} of the electrode surface, where a larger R_{ct} value suggests slower reaction kinetics.[47–50] The R_{ct} values of the Rh, GO, Pt/C, Rh@GO-SN,

Rh@GO-ST, and Rh@GO-PY modified GC electrodes were found to be 108.04, 401.15, 20.79, 69.58, 19.34, and 17.35 Ω, respectively. The lowest R_{ct} value of the Rh@GO-PY modified GC electrodes indicates that Rh@GO-PY has a higher electronic conductivity than the other electrocatalysts.

The electrocatalytic HER performance of Rh@GO-PY, Rh@GO-ST, Rh@GO-SN, GO, Rh and Pt/C was investigated by using *iR*-drop corrected linear sweep voltammetry (LSV) in 0.5 M H_2SO_4 solution at a scan rate of 5 mV s^{-1}, as shown in Fig. 9(b). The LSV curves clearly showed that Rh@GO-PY exhibits a lower overpotential value of 31 mV to attain 10 mA cm^{-2} current density, indicating the highest electrocatalytic activity for the HER. Whereas, Rh@GO-ST, Rh@GO-SN, Pt/C, Rh and GO catalysts required an overpotential value of 38, 76, 59, 118 and 552 mV, respectively to achieve a current density of 10 mA cm^{-2}. Thus, the electrocatalytic abilities of the prepared catalysts towards the HER followed the overall order of Rh@GO-PY > Rh@GO-ST > Pt/C > Rh@GO-SN > Rh > GO. Based on the aforementioned findings, the poor HER performance of GO can be attributed to its inherent limitations in active sites and electrical conductivity, which hinder efficient proton reduction. The Rh@GO-PY catalyst exhibited the lowest overpotential ($j =$ 10 mA cm^{-2}) and superior electrocatalytic performance for the HER, which might appear due to its high crystallinity (78.97%). Meanwhile, the Rh@GO-SN catalyst (crystallinity = 70.27%)
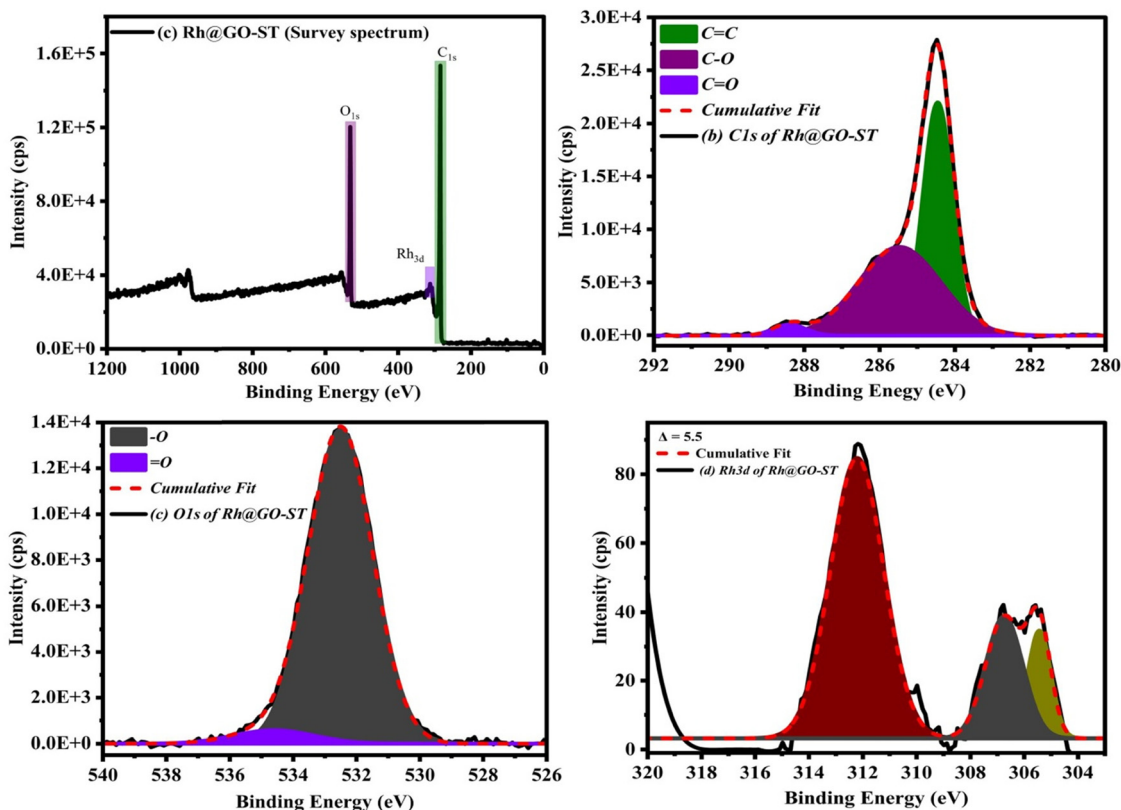
Fig. 7   XPS spectra of Rh@GO-ST: (a) survey spectrum, (b) C1s region, (c) O1s region, and (d) Rh3d region.

demonstrated moderate HER activity, surpassing GO due to the presence of Rh nanoparticles that enhanced its catalytic activity. The Rh@GO-ST catalyst displayed lower overpotential (j = 10 mA cm^{-2}) than the Rh@GO-SN catalyst, indicating enhanced catalytic activity that further exceeded the performance of GO. Although, Rh@GO-ST showed slightly lower crystallinity (69.31%) compared to Rh@GO-SN (70.27%), which might occur due to the presence of high atomic% of Rh nanoparticles in the Rh@GO-ST catalyst. As evidenced, Rh@GO-PY and Rh@GO-ST show excellent HER activity even
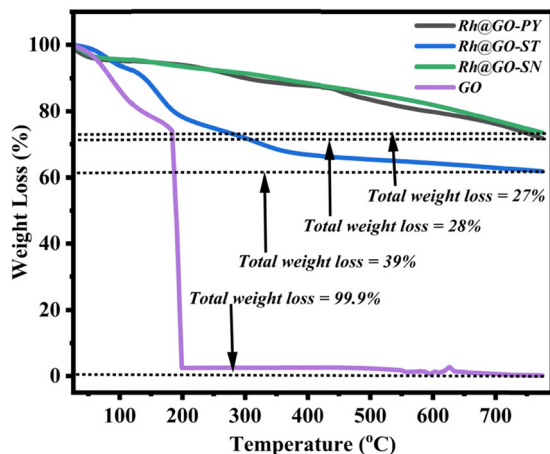

Fig. 8   TGA of GO, Rh@GO-SN, Rh@GO-ST and Rh@GO-PY.

better than Pt/C. Despite being a noble metal, pristine rhodium exhibits relatively low hydrogen evolution reaction (HER) activity compared to benchmark catalysts like platinum. This is largely due to its non-optimal hydrogen adsorption free energy (ΔG_{H^*}), which impairs the balance between hydrogen adsorption and desorption—both essential steps in HER catalysis. Rh tends to bind hydrogen either too strongly or too weakly on different crystallographic facets, reducing its overall catalytic efficiency. In addition, pristine Rh lacks sufficient surface area and active site density, further limiting its HER performance. As noted by Sheng et al., the intrinsic activity of Rh surfaces falls short when compared to Pt, emphasizing the need for support materials or structural modifications to enhance its catalytic behavior.[51]

To further elucidate the electrochemical performance of the HER, Tafel analysis was conducted in the kinetic region according to the following eqn (1):[52–54]

$$\eta = \left(\frac{2.303RT}{\alpha nF}\right)\log(j_0) - \left(\frac{2.303RT}{\alpha nF}\right)\log(j) \qquad (1)$$

where η is the overpotential, α is transfer co-efficient, j is current density, j_0 is the exchange current density and others represent their usual meanings.

A lower Tafel slope signifies that a smaller increase in overpotential results in a substantial increase in the reaction rate, indicating more favorable and efficient reaction kinetics. Specifically, for the HER, a lower Tafel slope suggests that the catalyst is more effective in promoting the formation of hydrogen gas from water,
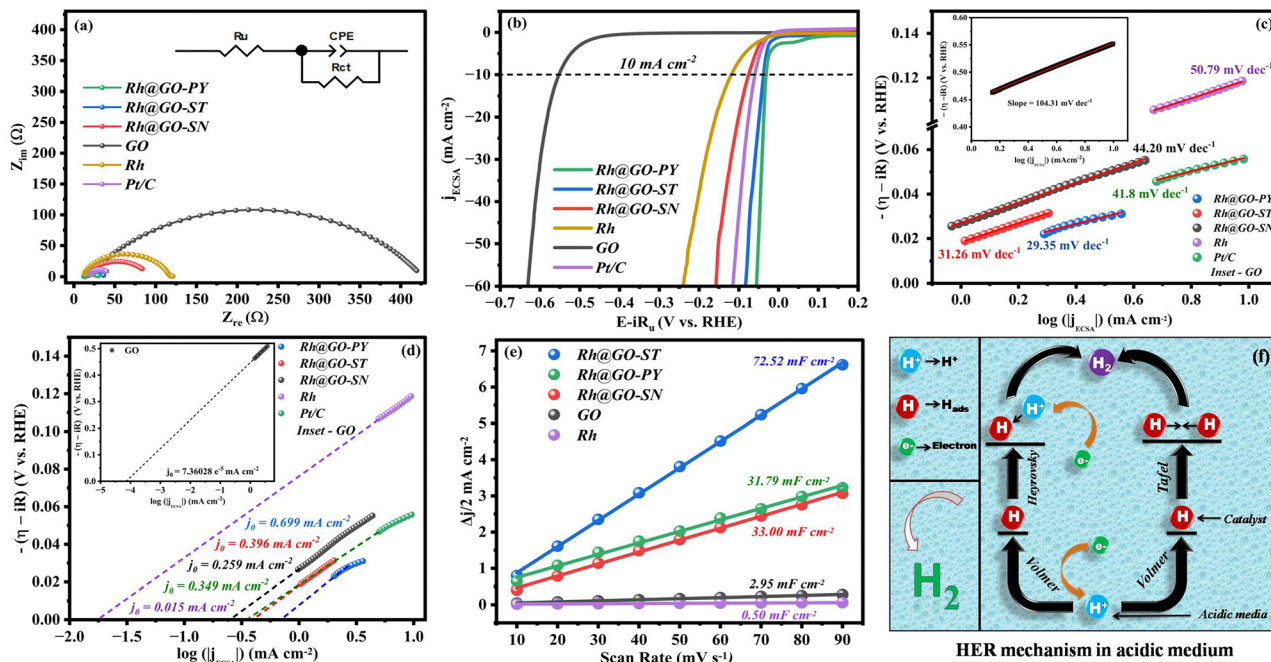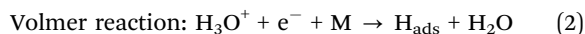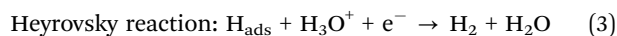
Fig. 9 Normalized electrochemical HER characterization of Rh@GO-PY, Rh@GO-ST, Rh@GO-SN, GO, Rh and Pt/C modified GCEs: (a) Nyquist plot in the frequency range of 0.1 Hz to 0.1 MHz, (b) *iR*-drop corrected LSV curves in 0.5 M H_2SO_4 solution at a scan rate of 5 mV s^{-1}, (c) corresponding Tafel plots, (d) Tafel line extrapolated to zero overpotential for the measurement of exchange current density, (e) $\Delta j/2$ *vs.* scan rate plots for C_{dl} measurement, and (f) schematic representation of the mechanism of the HER in acidic media.

implying that the reaction proceeds more easily with less energy input.[30,55] Therefore, catalysts with lower Tafel slopes are considered superior in terms of electrocatalytic activity and efficiency. Tafel plots were constructed from the LSV curves to analyze the kinetics of the HER on Rh@GO catalysts synthesized by different methods, as well as Pt/C, GO and Rh as shown in Fig. 9(c). The low Tafel slope of 29.35 mV dec^{-1} was recorded for the Rh@GO-PY catalyst, compared to 31.26, 41.80, 44.20, 50.79 and 104.31 mV dec^{-1} for Rh@GO-ST, Pt/C, Rh@GO-SN, Rh and GO, respectively. These results revealed that the Rh@GO-PY catalyst holds the highest electrocatalytic activity for the HER and followed the HER activity order of Rh@GO-PY > Rh@GO-ST > Pt/C > Rh@GO-SN > Rh > GO. This result is congruent with our earlier observation. Tafel analysis can also be applied to evaluate the insights of the reaction mechanism and identify the rate-determining step. To the best of our knowledge, the process of hydrogen evolution on the surface of an electrode in an acidic medium is mainly divided into two steps as represented in eqn (2)–(4).[56–60]

First step:

Volmer reaction: $H_3O^+ + e^- + M \rightarrow H_{ads} + H_2O$ (2)

Second step:

Heyrovsky reaction: $H_{ads} + H_3O^+ + e^- \rightarrow H_2 + H_2O$ (3)

or,

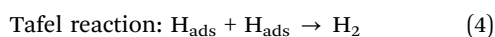Tafel reaction: $H_{ads} + H_{ads} \rightarrow H_2$ (4)

Fig. 9(f) gives a schematic representation of the mechanism of the HER in acidic media. Typically, the predominant HER mechanism of various catalysts can be identified by comparing the Tafel slope values: the Volmer reaction is the dominant rate-determining step when the Tafel slope is close to 118.2 mV dec^{-1}, whereas slope values close to 39.4 and 29.6 mV dec^{-1} represents that the Heyrovsky and Tafel reaction controls the rate-determining step of the HER, respectively.[58,61] The Tafel slope value of Rh@GO-PY and Rh@GO-ST was determined to be 29.35 and 31.26 mV dec^{-1}, indicating that both catalysts might follow the Volmer–Tafel reaction mechanism, while the Tafel reaction ($2H_{ads} \rightarrow H_2$) becomes the dominant rate-determining step of the HER in 0.5 M H_2SO_4 solution.[62,63] In contrast, the Rh@GO-SN (44.20 mV dec^{-1}), Rh (50.79 mV dec^{-1}) and GO (104.31 mV dec^{-1}) catalysts are expected to follow the Volmer–Heyrovsky reaction mechanism, while the Heyrovsky reaction ($H_{ads} + H_3O^+ + e^- \rightarrow H_2 + H_2O$) for Rh@GO-SN and the Volmer reaction ($H_3O^+ + e^- + M \rightarrow H_{ads} + H_2O$) for GO becomes the main rate-determining step.[58,63]

For constant proton activity, constant molecular hydrogen fugacity, and constant temperature, the electrocatalytic activity heavily depends on the composition and surface structure of the electrode. This activity is typically examined by the exchange current density (j_0), which is proportional to the reaction rate.[64] The exchange current density represents the anodic or cathodic current density flowing under dynamic equilibrium conditions. The exchange current density reflects the intrinsic activity of the electrocatalyst. A high exchange current density generally indicates excellent catalytic activity.[62–65] Fig. 9(d) shows the Tafel lines extrapolated to ($\eta = 0$) of the Rh@GO-PY, Rh@GO-ST, Rh@GO-SN, Pt/C, Rh and GO-modified GC electrodes. At the point of zero overpotential, the value of $\log(|j_{ECSA}|)$ is equal to $\log(j_0)$. It was observed that the Rh@GO-PY catalyst has the

highest exchange current density value of 0.699 mA cm^{-2} compared to Rh@GO-ST (0.396 mA cm^{-2}), Pt/C (0.349 mA cm^{-2}), Rh@GO-SN (0.259 mA cm^{-2}), Rh (0.015 mA cm^{-2}), and GO (7.36028 × 10^{-5} mA cm^{-2}). This result is congruent with our earlier observation.

The electrochemical double-layer capacitance (C_{dl}) is commonly employed to estimate the electrochemically active surface area (ECSA) of catalyst materials, with higher C_{dl} values typically indicating a larger ECSA. However, it is important to recognize that a material's catalytic performance is influenced not solely by its ECSA but also by its intrinsic activity, which encompasses factors such as electronic structure, surface chemistry, and the nature of active sites. Consequently, some materials may exhibit exceptional catalytic activity despite possessing a relatively low C_{dl}. This phenomenon can be attributed to several factors, such as intrinsic activity of the active sites, surface chemistry and functional groups, pore structure and accessibility, etc. The C_{dl} is influenced by factors beyond surface area, including the dielectric properties of the interface and ion adsorption characteristics. Variations in these properties can lead to discrepancies between C_{dl} and actual catalytic activity.[66,67] Fig. 9(e) presents the linear relationship between the capacitive current and scan rate (v), which reflects the C_{dl}, acting as an indicator for ECSA. The capacitive current values were obtained from the CV non-faradaic curves of the catalysts, as shown in Fig. S3 of ESI.† The C_{dl} of different catalysts follows the order Rh@GO-ST (72.52 mF cm^{-2}) > Rh@GO-SN (33.00 mF cm^{-2}) > Rh@GO-PY (31.79 mF cm^{-2}) > GO (2.95 mF cm^{-2}) > Rh (0.50 mF cm^{-2}). The observed variations in the hydrogen evolution reaction (HER) activity and electrochemical double-layer capacitance (C_{dl}) of Rh@GO-PY with respect to Rh@GO-ST and Rh@GO-SN can be attributed to differences in their synthesis methods, which influence the structural and electronic properties of the resulting composites. Pyrolysis involves high-temperature treatment that can lead to the formation of well-crystallized rhodium nanoparticles with strong interactions with the graphene oxide (GO) support. This process may enhance the electronic coupling between Rh and GO, optimizing the electronic structure of the composite and thereby improving intrinsic catalytic activity. Despite a potentially lower C_{dl}, indicating a smaller electrochemically active surface area (ECSA), the superior intrinsic activity of the active sites can result in enhanced overall HER performance of Rh@GO-PY as compared to Rh@GO-ST and Rh@GO-SN. This suggests that the quality and electronic properties of the active sites can outweigh the effects of surface area in determining catalytic efficiency. Hydrothermal synthesis typically yields materials with higher C_{dl} values due to the formation of nanostructures with increased surface area. However, the interaction between Rh nanoparticles and the GO support in this method may be weaker compared to pyrolysis, potentially leading to less optimal electronic properties and intrinsic activity. Therefore, even with a higher ECSA of Rh@GO-ST, the HER activity might not match that of Rh@GO-PY if the active sites are less catalytically efficient. Sonication-assisted synthesis can facilitate the dispersion of Rh nanoparticles on the GO sheets, potentially

increasing the surface area and C_{dl} of Rh@GO-SN. However, similar to the hydrothermal method, the electronic interactions and the nature of the active sites may not be as favorable as those achieved through pyrolysis. Consequently, the intrinsic activity of the catalyst may be lower, resulting in HER performance that does not scale directly with the increased C_{dl}. Similarly, pristine rhodium, despite having a lower C_{dl}, can exhibit higher HER activity than GO due to its inherently superior catalytic properties. Rhodium possesses favorable hydrogen adsorption energy, facilitating efficient HER processes. In contrast, GO itself is not catalytically active for the HER, but serves as a support material that can enhance the dispersion and utilization of metal nanoparticles. Therefore, the catalytic activity of Rh is intrinsically higher than that of GO, regardless of surface area and C_{dl} considerations. Overall, while a higher C_{dl} often correlates with increased surface area and potentially more active sites, the intrinsic activity of these sites, governed by factors such as electronic structure and metal–support interactions, plays a crucial role in determining overall HER performance. Thus, synthesis methods that optimize these intrinsic properties can produce catalysts with superior activity, even if their C_{dl} is comparatively lower.[19,68]

The comparative study of Rh@GO catalysts synthesized via sonication, solvothermal, and pyrolysis methods, alongside pristine graphene oxide (GO), offers valuable insights into how synthesis methods can tailor catalyst performance for the hydrogen evolution reaction (HER). The results highlight that the choice of synthesis method significantly influences the electrochemical properties and catalytic activity of the catalysts. Among the methods investigated, the pyrolysis method yields the highest HER activity, followed by solvothermal synthesis and sonication. This trend suggests that high-temperature treatment during pyrolysis promotes the formation of well-defined Rh nanoparticles on the GO support, thereby enhancing catalytic performance. The solvothermal method also enhances catalyst morphology and surface area compared to sonication, contributing to improved HER kinetics, albeit falling short of the catalytic activity achieved by the pyrolysis method. Pristine GO serves as a reference material with minimal HER activity due to its limited active sites and electrical conductivity. Incorporating Rh nanoparticles via different synthesis methods effectively mitigates these shortcomings, enhancing the catalytic performance of GO-based catalysts. These findings underscore the importance of optimizing synthesis conditions to design efficient electrocatalysts for the HER. The demonstrated effectiveness of the Rh@GO catalysts, particularly those synthesized via solvothermal and pyrolysis methods holds promise for various renewable energy applications such as water electrolysis and hydrogen fuel cells.[69–72] Table S2 in the ESI† presents a comparison of the HER performances of Rh@GO-PY, Rh@GO-ST and Rh@GO-SN with some previously reported Rh-based electrocatalysts at 10 mA cm^{-2} current density in 0.5 M H$_2$SO$_4$.

Electrocatalysts used in practical applications like water electrolyzers are exposed to continuous redox cycling and harsh potential conditions. Therefore, assessing both short-term stability and long-term durability under constant potential is
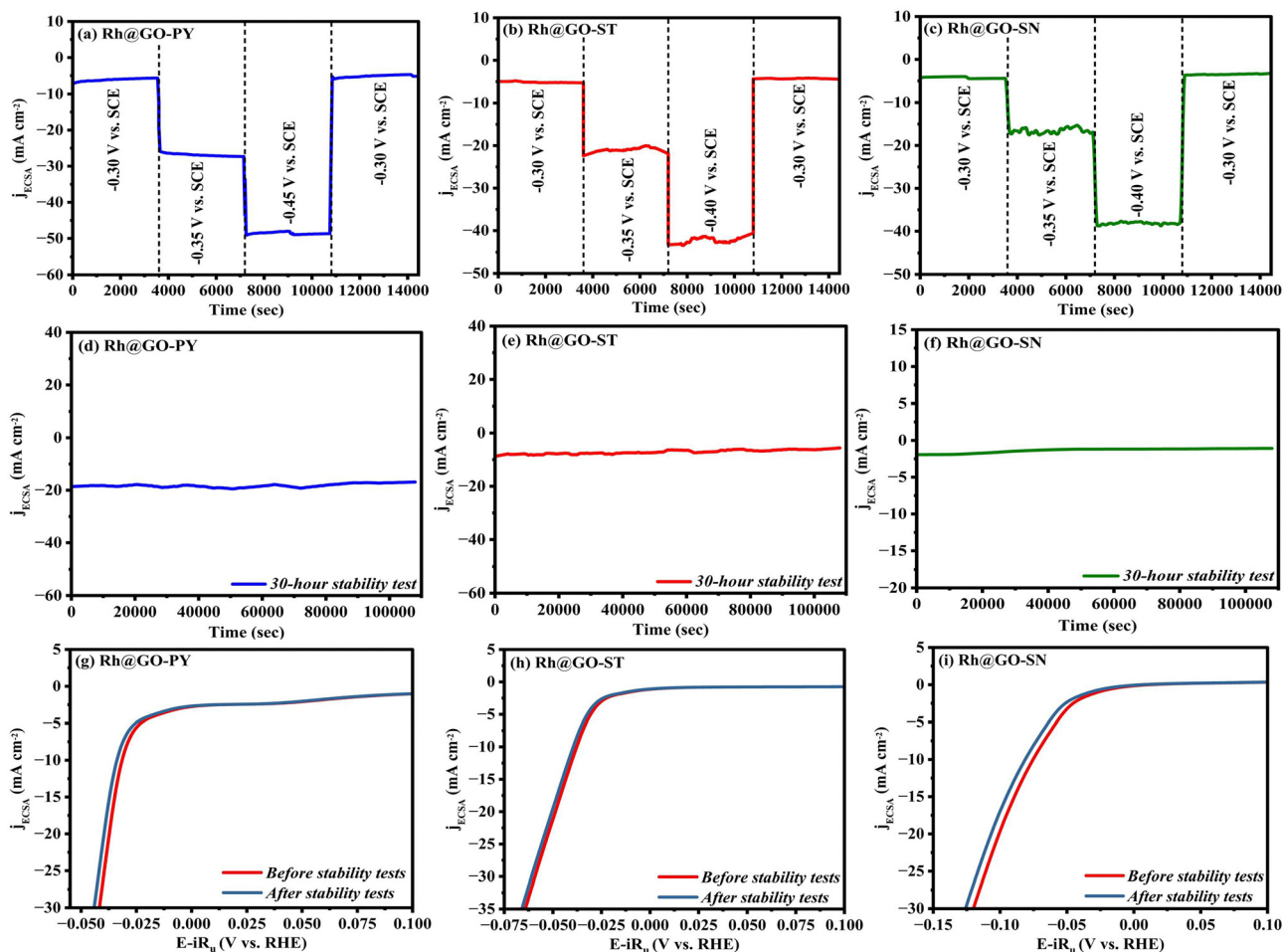
Fig. 10 Stability and durability tests of the Rh@GO electrocatalysts (Rh@GO-PY, Rh@GO-ST and Rh@GO-SN) in 0.5 M H_2SO_4 solution by using a chronoamperometric (CA) i–t curve: (a)–(c) durability tests at varying potentials (-0.30, -0.35, -0.40 or -0.45 V $vs.$ SCE, and finally returning to -0.30 V $vs.$ SCE), (d)–(f) 30-hour stability tests, and (g)–(i) LSV curves before and after durability and stability tests at a scan rate of 5 mV s^{-1}.

critical to ensure sustained performance without significant degradation. The chronoamperometric (CA) i–t curve technique was used to check the stability and durability of the catalysts. The durability of Rh@GO electrocatalysts (Rh@GO-PY, Rh@GO-ST and Rh@GO-SN) was evaluated through exposure to varying potentials of -0.30, -0.35, -0.40 or -0.45 V $vs.$ SCE, and finally returning to -0.30 V $vs.$ SCE, as shown in Fig. 10(a)–(c). Despite undergoing 1-h intervals at each step, only minimal fluctuations in current density were observed. Significantly, upon returning the potential to its starting value, the current density promptly returned to its starting point, indicating a notable degree of reversibility. Fig. 10(d)–(f) presents the stability evaluation of the Rh@GO electrocatalysts (Rh@GO-PY, Rh@GO-ST and Rh@GO-SN) for a time duration of 30 h each. During this period, the catalysts maintained a stable current density with minimal fluctuations, demonstrating their strong electro-catalytic durability. Rh@GO-PY has superior stability as compared to Rh@GO-ST and Rh@GO-SN.

Fig. 10(g)–(i) presents HER polarization curves (iR-corrected) for three Rh@GO electrocatalysts (Rh@GO-PY, Rh@GO-ST, and Rh@GO-SN) before and after stability testing, plotted as current

density (j_{ECSA}) $versus$ potential ($E - iR_u$ $vs.$ RHE). These measurements are used to assess the electrocatalytic performance retention after prolonged electrochemical operation. It is observed that in the case of Rh@GO-PY (Fig. 10(g)), the polarization curve after stability testing shows minimal deviation from the initial curves. However, the change is modest, suggesting good electrochemical durability. In the case of Rh@GO-ST (Fig. 10(h)), the curves before and after stability testing are nearly overlapping, indicating excellent retention of HER activity. This suggests that Rh@GO-ST remains electrochemically stable, with minimal degradation under extended operation. Rh@GO-SN (Fig. 10(i)) also shows minimal deviation between the initial and after activity curves. The negligible shift further confirms high durability and stable catalytic performance.

4. Conclusion

Based on the findings, it is evident that the synthesis method plays a vital role in dictating the HER performance of Rh@GO

catalysts. Among all variants, the pyrolysis-derived Rh@GO catalyst exhibits the most superior HER activity, as demonstrated by its lowest overpotential, smallest Tafel slope, and minimal charge transfer resistance, indicating enhanced proton reduction kinetics and improved electron transport. The solvothermal-synthesized Rh@GO also performs well, closely following the pyrolyzed sample; whereas the sonication-based Rh@GO shows comparatively inferior HER activity due to less efficient Rh dispersion and weaker interaction with GO. In comparison, pristine Rh nanoparticles exhibit moderate catalytic activity but suffer from nanoparticle agglomeration and limited surface area. Graphene oxide (GO) alone shows very poor HER activity due to its inherently low conductivity and lack of active sites. The pyrolysis and solvothermal Rh@GO composites emerge as cost-effective, stable, and active alternatives to Pt/C, with enhanced catalytic performance than Pt/C resulting from improved Rh dispersion, strong Rh–GO interaction, and conductive support, underscoring their potential in scalable hydrogen production systems.

Data availability

Data is available in the ESI† and main manuscript. Furthermore, on reasonable request the authors may provide data.

Conflicts of interest

There are no conflicts to declare.

Acknowledgements

References

1 Clean energy can fuel the future—and make the world healthier, *Nature*, 2023, **620**, 245.

2 T. Cai, D. Zhao, Y. Sun, S. Ni, W. Li, D. Guan and B. Wang, Evaluation of NO emissions characteristics in a CO2-Free micro-power system by implementing a perforated plate, *Renewable Sustainable Energy Rev.*, 2021, **145**, 111150.

3 A. K. Cover, A. Álvarez, O. Barānovs, F. Bastarrica, O. Bogdanova, F. Carlos, N. Carvalho, L. Chiara, V. Dombrovskis, I. Estrada, F. Ferrés, P. Ferreira, D. Fragkiadakis, K. Fragkiadakis, P. Frade, K. Gičevskis, J. Gomes, M. Gonçalves, E. Groza, A. Humbatov, G. Irrazabal, M. Iten, I. Karpoviča, K. Kishore, O. Krasnopjorovs, T. Liepnieks, J. Mercant, H. Millers, R. Oļekšijs, L. Paroussos, A. Perroni, K. Pigens, A. Piebalgs, H. Pombeiro, E. Rozenfelds, J. Salmiņš, H. Bruno, I. Santos, E. Skribāne, A. Smiltāns, I. Sousa, A. Šteinbuka, G. Tukulis, K. Valdmanis, A. Viskuba, F. Wilkinson, R. Čudars and A. Bogdanova, *Towards climate neutrality: Economic impacts, opportunities and risks*, 2023.

4 Global Energy Transition a roadmap to 2050, **https://www.irena.org/publications/2018/Apr/Global-Energy-Transition-A-Roadmap-to-2050**, (accessed May 17, 2025).

5 H. Song, S. Luo, H. Huang, B. Deng and J. Ye, Solar-Driven hydrogen production: recent advances, challenges, and future perspectives, *ACS Energy Lett.*, 2022, **7**, 1043–1065.

6 P. J. Megía, A. J. Vizcaíno, J. A. Calles and A. Carrero, Hydrogen Production Technologies: From Fossil Fuels toward Renewable Sources. A Mini Review, *Energy Fuels*, 2021, **35**, 16403–16415.

7 A. I. Osman, M. Nasr, A. S. Eltaweil, M. Hosny, M. Farghali, A. S. Al-Fatesh, D. W. Rooney and E. M. A. El-Monaem, Advances in hydrogen storage materials: harnessing innovative technology, from machine learning to computational chemistry, for energy storage solutions, *Int. J. Hydrogen Energy*, 2024, **67**, 1270–1294.

8 S. Kogularasu, Y. Lee, B. Sriram, S. Wang, M. George, G. Chang-Chien and J. Sheu, Unlocking Catalytic potential: Exploring the impact of thermal treatment on enhanced electrocatalysis of nanomaterials, *Angew. Chem., Int. Ed.*, 2023, **63**(1), e202311806.

9 V. Vij, S. Sultan, A. M. Harzandi, A. Meena, J. N. Tiwari, W.-G. Lee, T. Yoon and K. S. Kim, Nickel-Based Electrocatalysts for Energy-Related applications: oxygen reduction, oxygen evolution, and hydrogen evolution reactions, *ACS Catal.*, 2017, **7**, 7196–7225.

10 J. Barrio, A. Pedersen, S. Favero, H. Luo, M. Wang, S. Ch Sarma, J. Feng, L. T. T. Ngoc, S. Kellner, A. Y. Li, A. B. J. Sobrido and M.-M. Titirici, Bioinspired and bioderived aqueous electrocatalysis, *Chem. Rev.*, 2022, **123**, 2311–2348.

11 V. Palma, D. Barba, M. Cortese, M. Martino, S. Renda and E. Meloni, Microwaves and Heterogeneous catalysis: A review on selected catalytic processes, *Catalysts*, 2020, **10**, 246.

12 D. Xu, K. Li, B. Jia, W. Sun, W. Zhang, X. Liu and T. Ma, Electrocatalytic CO2 reduction towards industrial applications, *Carbon Energy*, 2022, **5**(1), e230.

13 A. Begum, M. Bose and G. Moula, Graphene supported rhodium nanoparticles for enhanced electrocatalytic hydrogen evolution reaction, *Sci. Rep.*, 2019, **9**, 17027.

14 J. Golubović, L. Rakočević, N. Latas, M. Varničić, V. Rajić and S. Štrbac, Enhanced hydrogen evolution catalysis on Rh

nanoparticles with low loading on graphene nanoplatelets, *Appl. Surf. Sci.*, 2024, **672**, 160805.

15 D. C. Marcano, D. V. Kosynkin, J. M. Berlin, A. Sinitskii, Z. Sun, A. Slesarev, L. B. Alemany, W. Lu and J. M. Tour, Improved synthesis of graphene oxide, *ACS Nano*, 2010, **4**, 4806–4814.

16 S. N. Alam, N. Sharma and L. Kumar, Synthesis of graphene oxide (GO) by modified hummers method and its thermal reduction to obtain reduced graphene oxide (RGO)*, *Graphene*, 2017, **06**, 1–18.

17 A. Faiz, C. A. C. Azurahanim, S. A. Raba'ah and M. Z. Ruzniza, Low cost and green approach in the reduction of graphene oxide (GO) using palm oil leaves extract for potential in industrial applications, *Results Phys.*, 2020, **16**, 102954.

18 J. Yan, T. Wei, B. Shao, F. Ma, Z. Fan, M. Zhang, C. Zheng, Y. Shang, W. Qian and F. Wei, Electrochemical properties of graphene nanosheet/carbon black composites as electrodes for supercapacitors, *Carbon*, 2010, **48**, 1731–1737.

19 Y. Kang, Q. Xue, P. Jin, J. Jiang, J. Zeng and Y. Chen, Rhodium Nanosheets–Reduced Graphene oxide hybrids: a highly active Platinum-Alternative electrocatalyst for the methanol oxidation reaction in alkaline media, *ACS Sustainable Chem. Eng.*, 2017, **5**, 10156–10162.

20 W. Shen, L. Ge, Y. Sun, F. Liao, L. Xu, Q. Dang, Z. Kang and M. Shao, Rhodium Nanoparticles/F-Doped Graphene composites as multifunctional electrocatalyst superior to PT/C for hydrogen evolution and formic acid oxidation reaction, *ACS Appl. Mater. Interfaces*, 2018, **10**, 33153–33161.

21 H. Chang, Y. Lei, D. He, X. Sheng, Z. Song and X. Feng, Strongly Coupled Rhodium/Graphene Hybrids for H2O2 Oxidation with Ultra-Low Potential and Enhanced Activity, *ChemElectroChem*, 2014, **1**, 1480–1483.

22 S. Thakur and N. Karak, Green reduction of graphene oxide by aqueous phytoextracts, *Carbon*, 2012, **50**, 5331–5339.

23 M. S. Dresselhaus, A. Jorio, M. Hofmann, G. Dresselhaus and R. Saito, Perspectives on Carbon Nanotubes and Graphene Raman Spectroscopy, *Nano Lett.*, 2010, **10**, 751–758.

24 W. Lu, J.-B. Baek and L. Dai, *Carbon nanomaterials for advanced energy systems*, 2015, pp. 1–448.

25 Y. Su, J. Du, D. Sun, C. Liu and H. Cheng, Reduced graphene oxide with a highly restored π-conjugated structure for inkjet printing and its use in all-carbon transistors, *Nano Res.*, 2013, **6**, 842–852.

26 D. Yang, A. Velamakanni, G. Bozoklu, S. Park, M. Stoller, R. D. Piner, S. Stankovich, I. Jung, D. A. Field, C. A. Ventrice and R. S. Ruoff, Chemical analysis of graphene oxide films after heat and chemical treatments by X-ray photoelectron and Micro-Raman spectroscopy, *Carbon*, 2008, **47**, 145–152.

27 B. R. Sathe, Rhodium nanoparticle–carbon nanosphere hybrid material as an electrochemical hydrogen sensor, *RSC Adv.*, 2013, **3**, 5361.

28 S. S. Narwade, B. B. Mulik, S. M. Mali and B. R. Sathe, Silver nanoparticles sensitized C60(Ag@C60) as efficient electrocatalysts for hydrazine oxidation: Implication for hydrogen generation reaction, *Appl. Surf. Sci.*, 2016, **396**, 939–944.

29 J. Song, L. Xu, R. Xing, Q. Li, C. Zhou, D. Liu and H. Song, Synthesis of AU/Graphene oxide composites for selective and sensitive electrochemical detection of ascorbic acid, *Sci. Rep.*, 2014, **4**, 7515.

30 S. S. Narwade, S. M. Mali, V. S. Sapner and B. R. Sathe, Graphene Oxide Decorated with Rh Nanospheres for Electrocatalytic Water Splitting, *ACS Appl. Nano Mater.*, 2020, **3**, 12288–12296.

31 N. G. De Barros, A. C. G. Neto, K. B. Vaccioli, H. R. V. Angulo, L. G. De Andrade, E. Silva, S. M. Toffoli and T. S. Valera, Graphene Oxide: A comparison of reduction Methods, *C*, 2023, **9**, 73.

32 D. Skoda, J. Vilcakova, R. S. Yadav, B. Hanulikova, T. Capkova, M. Jurca, M. Urbanek, P. Machac, L. Simonikova, J. Antos and I. Kuritka, Nickel nanoparticle–decorated reduced graphene oxide via one-step microwave-assisted synthesis and its lightweight and flexible composite with Polystyrene-*block*-poly-(ethylene-ran-butylene)-*block*-polystyrene polymer for electromagnetic wave shielding application, *Adv. Compos. Hybrid Mater.*, 2023, **6**, 113.

33 Q. Lei, J. Wang and A. Misra, Mechanical behavior of Al–AL2CU–SI and Al–AL2CU eutectic alloys, *Crystals*, 2021, **11**, 194.

34 H. Zheng, X. Huang, H. Gao, W. Dong, G. Lu, X. Chen and G. Wang, Decorating cobalt phosphide and rhodium on reduced graphene oxide for high-efficiency hydrogen evolution reaction, *J. Energy Chem.*, 2018, **34**, 72–79.

35 M. Sookhakian, G. B. Tong and Y. Alias, *In-Situ* Electrodeposition of Rhodium nanoparticles Anchored on Reduced Graphene Oxide nanosheets as an Efficient Oxygen Reduction Electrocatalyst, *Appl. Organomet. Chem.*, 2020, **34**(3), e5370.

36 R. Al-Gaashani, A. Najjar, Y. Zakaria, S. Mansour and M. A. Atieh, XPS and structural studies of high quality graphene oxide and reduced graphene oxide prepared by different chemical oxidation methods, *Ceram. Int.*, 2019, **45**, 14439–14448.

37 L. S. Kibis, A. I. Stadnichenko, S. V. Koscheev, V. I. Zaikovskii and A. I. Boronin, XPS study of nanostructured rhodium oxide film comprising RH4+ species, *J. Phys. Chem. C*, 2016, **120**, 19142–19150.

38 Y. Chen, R. Zhang, Z. Chen, J. Liao, X. Song, X. Liang, Y. Wang, J. Dong, C. V. Singh, D. Wang, Y. Li, F. D. Toste and J. Zhao, Heterogeneous rhodium Single-Atom-Site catalyst enables chemoselective carbene N–H bond insertion, *J. Am. Chem. Soc.*, 2024, **146**, 10847–10856.

39 J. F. Moulder, *Handbook of X-Ray Photoelectron Spectroscopy*, 1995.

40 X. Mei, Q. Yan, P. Lu, J. Wang, Y. Cui, Y. Nie, A. Umar and Q. Wang, Synthesis of Pt/K2CO3/MgAlOx–reduced graphene oxide hybrids as promising NOx storage–reduction catalysts with superior catalytic performance, *Sci. Rep.*, 2017, **7**, 42862.

41 V. Halperin, G. E. Shter, V. Gelman, D. M. Peselev, M. Mann-Lahav and G. S. Grader, Catalytic activity of electrospun Ag and Ag/carbon composite fibres in partial methanol oxidation, *Catal. Sci. Technol.*, 2014, **5**, 1153–1162.

42 R. Xing and W. S. W. Ho, Crosslinked polyvinylalcohol–polysiloxane/fumed silica mixed matrix membranes

containing amines for CO2/H2 separation, *J. Membr. Sci.*, 2010, **367**, 91–102.

43 T. Wang, L.-X. Wang, D.-L. Wu, W. Xia and D.-Z. Jia, Interaction between Nitrogen and Sulfur in Co-Doped Graphene and Synergetic Effect in Supercapacitor, *Sci. Rep.*, 2015, **5**, 9591.

44 M. Ugalde, E. Chavira, M. T. Ochoa-Lara, I. A. Figueroa, C. Quintanar and A. Tejeda, Synthesis by microwaves of bimetallic Nano-Rhodium-Palladium, *J. Nanotechnol.*, 2013, 1–9.

45 L. Huang, P. Zhu, G. Li, D. Lu, R. Sun and C. Wong, Core–shell SiO2@RGO hybrids for epoxy composites with low percolation threshold and enhanced thermo-mechanical properties, *J. Mater. Chem. A*, 2014, **2**, 18246–18255.

46 S. Anantharaj and S. Noda, iR drop correction in electrocatalysis: everything one needs to know!, *J. Mater. Chem. A*, 2022, **10**, 9348–9354.

47 M. N. Islam, J. Ahmed, M. Faisal, J. S. Algethami, K. Aoki, Y. Nagao, F. A. Harraz and M. A. Hasnat, Efficient electrocatalytic hydrogen evolution reaction on CUO immobilized Stainless-Steel electrode prepared by the SILAR method, *ChemistrySelect*, 2023, **8**(28), e20231077.

48 M. N. Islam, M. Ahsan, K. Aoki, Y. Nagao, A. E. Alsafrani, H. M. Marwani, A. Almahri, M. M. Rahman and M. A. Hasnat, Development of CuNi immobilized Pt surface to minimize nitrite evolution during electrocatalytic nitrate reduction in neutral medium, *J. Environ. Chem. Eng.*, 2023, **11**, 111149.

49 M. N. Islam, A. Y. Abir, J. Ahmed, M. Faisal, J. S. Algethami, F. A. Harraz and M. A. Hasnat, Electrocatalytic oxygen reduction reaction at FeS2-CNT/GCE surface in alkaline medium, *J. Electroanal. Chem.*, 2023, **941**, 117568.

50 J. Ahmed, Md. N. Islam, M. Faisal, J. S. Algethami, Md. M. Hasan, I. A. Siddiquey, M. A. Hasnat and F. A. Harraz, Electrocatalytic investigation of H2O2 reduction and sensing performance using sulfide modified Au/Pt electrode in alkaline medium, *Colloids Surf., A*, 2023, **682**, 132926.

51 A. A. Feidenhans'l, Y. N. Regmi, C. Wei, D. Xia, J. Kibsgaard and L. A. King, Precious Metal Free Hydrogen Evolution Catalyst Design and Application, *Chem. Rev.*, 2024, **124**, 5617–5667.

52 A. J. Bard, L. R. Faulkner and H. S. White, *Electrochemical methods: Fundamentals and Applications*, John Wiley & Sons, 2022.

53 P. Kairy, Md. N. Islam, M. Ahsan, Md. A. Rashed, A. E. Alsafrani, H. M. Marwani, A. Almahri, M. M. Rahman and M. A. Hasnat, Electrocatalytic reduction of Cr(VI) on gold-based electrodes in acidic medium: A systematic approach to chromium detection, *Electrochim. Acta*, 2023, **467**, 142938.

54 H. Begum, Md. N. Islam, S. B. Aoun, J. A. Safwan, S. S. Shah, Md. A. Aziz and M. A. Hasnat, Electrocatalytic reduction of nitrate ions in neutral medium at coinage metal-modified platinum electrodes, *Environ. Sci. Pollut. Res.*, 2022, **30**, 34904–34914.

55 S. Anantharaj and S. Noda, Dos and don'ts in screening water splitting electrocatalysts, *Energy Adv.*, 2022, **1**, 511–523.

56 K. Krischer and E. R. Savinova, Fundamentals of Electrocatalysis, *Handbook of Heterogeneous Catalysis*, 2008, pp. 1873–1905.

57 P. Quaino, F. Juarez, E. Santos and W. Schmickler, Volcano plots in hydrogen electrocatalysis – uses and abuses, *Beilstein J. Nanotechnol.*, 2014, **5**, 846–854.

58 Y. Zheng, Y. Jiao, M. Jaroniec and S. Z. Qiao, Advancing the Electrochemistry of the Hydrogen-Evolution Reaction through Combining Experiment and Theory, *Angew. Chem., Int. Ed.*, 2014, **54**, 52–65.

59 X. Jin, J. Li, Y. Cui, X. Liu, X. Zhang, J. Yao and B. Liu, CU3P–NI2P hybrid hexagonal nanosheet arrays for efficient hydrogen evolution reaction in alkaline solution, *Inorg. Chem.*, 2019, **58**, 11630–11635.

60 Z. Lv, D. Liu, W. Tian and J. Dang, Designed synthesis of WC-based nanocomposites as low-cost, efficient and stable electrocatalysts for the hydrogen evolution reaction, *CrystEngComm*, 2020, **22**, 4580–4590.

61 Q. Lu, Y. Yu, Q. Ma, B. Chen and H. Zhang, 2D Transition-Metal-Dichalcogenide-Nanosheet-Based composites for photocatalytic and electrocatalytic hydrogen evolution reactions, *Adv. Mater.*, 2015, **28**, 1917–1933.

62 R. Zhang, X. Wang, S. Yu, T. Wen, X. Zhu, F. Yang, X. Sun, X. Wang and W. Hu, Ternary NICO2PX nanowires as PH-Universal electrocatalysts for highly efficient hydrogen evolution reaction, *Adv. Mater.*, 2016, **29**(9), 1605502.

63 Z. Chen, X. Duan, W. Wei, S. Wang and B.-J. Ni, Recent advances in transition metal-based electrocatalysts for alkaline hydrogen evolution, *J. Mater. Chem. A*, 2019, **7**, 14971–15005.

64 P. Yu, F. Wang, T. A. Shifa, X. Zhan, X. Lou, F. Xia and J. He, Earth abundant materials beyond transition metal dichalcogenides: A focus on electrocatalyzing hydrogen evolution reaction, *Nano Energy*, 2019, **58**, 244–276.

65 S. Anantharaj and S. Noda, How properly are we interpreting the Tafel lines in energy conversion electrocatalysis?, *Mater. Today Energy*, 2022, **29**, 101123.

66 A. M. Schott, P. M. Schneider, K.-T. Song, H. Yu, R. Götz, F. Haimerl, E. Gubanova, J. Zhou, T. O. Schmidt, Q. Zhang, V. Alexandrov and A. S. Bandarenka, How to assess and predict electrical double layer properties. Implications for electrocatalysis, *Chem. Rev.*, 2024, **124**, 12391–12462.

67 S. Anantharaj, H. Sugime and S. Noda, Why shouldn't double-layer capacitance (Cdl) be always trusted to justify faradaic electrocatalytic activity differences?, *J. Electroanal. Chem.*, 2021, **903**, 115842.

68 M. K. Kundu, R. Mishra, T. Bhowmik and S. Barman, Rhodium metal–rhodium oxide (Rh–Rh2O3) nanostructures with Pt-like or better activity towards hydrogen evolution and oxidation reactions (HER, HOR) in acid and base: correlating its HOR/HER activity with hydrogen binding energy and oxophilicity of the catalyst, *J. Mater. Chem. A*, 2018, **6**, 23531–23541.

69 J. Shen, L. Yang, K. Hu, W. Luo and G. Cheng, Rh nanoparticles supported on graphene as efficient catalyst for hydrolytic dehydrogenation of amine boranes for chemical

hydrogen storage, *Int. J. Hydrogen Energy*, 2014, **40**, 1062–1070.

70 H. Sachdeva, Recent advances in the catalytic applications of GO/rGO for green organic synthesis, *Green Process Synth.*, 2020, **9**, 515–537.

71 H. Su and Y. H. Hu, Recent advances in graphene-based materials for fuel cell applications, *Energy Sci. Eng.*, 2020, **9**, 958–983.

72 X. Qin, O. Ola, J. Zhao, Z. Yang, S. K. Tiwari, N. Wang and Y. Zhu, Recent progress in Graphene-Based electrocatalysts for hydrogen evolution reaction, *Nanomaterials*, 2022, **12**, 1806.